

# 12

## Atomistic Reaction Pathway Sampling: The Nudged Elastic Band Method and Nanomechanics Applications

Ting Zhu<sup>a</sup>, Ju Li<sup>b,c</sup>, and Sidney Yip<sup>b,e</sup>

<sup>a</sup>*Georgia Institute of Technology*

<sup>b</sup>*Massachusetts Institute of Technology*

~~<sup>c</sup>*Massachusetts Institute of Technology*~~

### 12.1 Introduction

Two of the central recurring themes in nanomechanics are strength and plasticity [1–3]. They are naturally coupled because plastic deformation is a major strength-determining mechanism and understanding the resistance to deformation (strength) is a principal motivation for studying plasticity. Many phenomena of interest in mechanics can be discussed in the framework of microstructural evolution of a system where defects like cracks and dislocations are formed and evolve interactively. Microstructure evolution at the nanoscale is particularly relevant from the standpoint of probing unit processes of deformation, such as advancement of a crack front by a lattice unit or propagation of a dislocation core by a Burgers vector. These atomic-level details can reveal the mechanisms of deformation, which are the essential inputs to describing microstructure evolution at the mesoscale – the next length and time scales. This hierarchical relation is the essence of multiscale modeling and simulation paradigm [4–6].

The purpose of this chapter is to discuss the atomistic approach to describe the evolution of crystalline defects [1–3,6]. We focus on a method, which is becoming widely used, that allows one to track the microstructure evolution through the sampling of a

replace  
"a Burgers vector" by  
"a lattice vector"

minimum-energy path (MEP) [7–9]. This path describes the variation of the energy of the system as it moves through a unit process reaction from an initial to a final state. The sampling also produces a reaction coordinate which is a collective coordinate that can be **transformed into** system atomic configurations along the reaction pathway. The determination of the MEP, therefore, provides two pieces of valuable information: the saddle point energy of the reaction, which is the activation energy required for the reaction to occur, and the atomic configurations at the saddle point, which can reveal the molecular mechanism associated with the unit process. Several case studies are then discussed to illustrate the applicability of the sampling method, known as the nudged elastic band (NEB) [7–9], and the MEP that it can produce for each unit process. For microstructure evolution over extended time intervals the system still can be characterized by reaction pathways, although the concept of a unit process is no longer appropriate. For these problems, other atomistic sampling methods can be used to determine the appropriate transition-state pathway (TSP) trajectories which are effectively an ordered sequence of MEPs. Such studies are only emerging. While they are beyond the scope of the present discussion, we will nevertheless provide a brief outlook on some recent developments [10].

The chapter is laid out as follows. Motivation and brief introductions to reaction pathway sampling, the NEB method of determining the MEP, and transition-state theory of activated processes are covered in Section 12.1. Section 12.2 deals with the NEB method as applied to stress-driven unit processes. Section 12.3 describes the atomistic results for several scenarios: dislocation emission at a crack tip, interaction between a silica nanorod and a water molecule, twinning effects at the nanoscale, temperature and strain-rate sensitivity, and size effects. Section 12.4 is a concluding outlook on microstructure evolution at longer times from the standpoint of atomistic sampling methods and challenging problems in the area of materials ageing.

### 12.1.1 Reaction Pathway Sampling in Nanomechanics

We are primarily concerned here with the modeling and simulation of unit processes in nanoscale deformation. The nucleation and evolution of defects will be described in terms of reaction pathways with specified initial and final states. We will focus on a particular atomistic method of sampling (determined by simulation) the defect reaction pathway, a method that is known as the NEB [7–9]. With this method one can obtain the MEP, which describes the variation in system energy along a reaction coordinate. The determination of the MEP allows one to find the energy barrier for the reaction. Since a one-to-one relation exists between the reaction coordinate and the atomic configurations of the system, the MEP also allows us to study the atomic configurations at the saddle point. Such details are needed to establish the unit mechanism of deformation.

### 12.1.2 Extending the Time Scale in Atomistic Simulation

Atomistic simulations, of which molecular dynamics (MD) is the primary method, are known for their time-scale limitations. The limitations usually appear in one of two ways. The explicit limitation is the time interval that a simulation can cover, while a more implicit limitation is the rate of change that one can impose externally on the system.

MD studies, as direct simulation of Newtonian dynamics, cannot extend over times longer than nanoseconds without using acceleration techniques [11] in conjunction with transition-state theory (see Section 12.1.3). MD gives directly the time responses of the system to external perturbations (imposed in discrete steps); the effective rates of perturbation associated with the simulation are invariably orders of magnitude higher than what can be practically imposed in experiments or in nature. The reason is simply because the basic time step in the integration of Newton's equations of motion is restricted to femtoseconds. The extreme rate of perturbation of all MD simulations, therefore, calls into question the physical meaning of the mechanisms revealed by simulation in comparison with rate-dependent responses of systems studied experimentally.

### 12.1.3 Transition-State Theory

Many of the inelastic deformations in solids, including dislocation slip, twinning, and phase transformation, occur by the thermally activated processes of atomic rearrangement. According to transition-state theory [12,13], the rate of a thermally activated process can be estimated according to

$$v = v_0 \exp\left(-\frac{Q(\sigma, T)}{k_B T}\right) \quad (12.1)$$

where  $v_0$  is the trial frequency,  $k_B$  is the Boltzmann constant, and  $Q$  is the activation free energy whose magnitude is controlled by the local stress  $\sigma$  and temperature  $T$ .

To develop a quantitative sense of Equation (12.1), it is instructive to consider some numbers. The physical trial frequency  $v_0$  is typically on the order of  $10^{11} \text{ s}^{-1}$ , as dictated by the atomic vibration. In order for a thermally activated process observable in a typical laboratory experiment, the rate  $v$  should be of the order of say  $10^{-2} \text{ s}^{-1}$ , so that the activation energy needs to be around  $30k_B T$ . As such, a thermally activated process with an energy barrier of  $\sim 0.7 \text{ eV}$  would be relevant to the laboratory experiment at room temperature (the corresponding thermal energy  $k_B T \approx 1/40 \text{ eV}$ ).

Clearly, the activation free energy  $Q$  in Equation (12.1) is a quantity of central importance for determining the kinetic rate within transition-state theory. Its value depends on the specific activation processes of atomic rearrangement, and is a function of stress, temperature, and system size, and so on. To a first approximation,  $Q$  can be estimated by the 0 K energy barrier, which can be effectively evaluated by using the NEB method.

## 12.2 The NEB Method for Stress-Driven Problems

### 12.2.1 The NEB method

The NEB method is a chain-of-states approach of finding the MEP on the potential energy surface (PES). In configuration space, each point represents one configuration of atoms in the system. This configuration has a 0 K potential energy, which can be evaluated by using the empirical interatomic potential or first-principles method [5]. The PES is the surface of the potential energy of each point in configuration space. In general, there are basins, ridges, local minima and saddle points on the PES. The MEP is the lowest energy path for a rearrangement of a group of atoms from one stable configuration to another; that

is, from one local energy minimum to another [7]. The potential energy maximum along the MEP is the saddle-point energy which gives the activation energy barrier; that is,  $Q$  in Equation (12.1).

In an NEB calculation, the initial and final configurations should be first determined by using energy minimization. Then, a discrete band, consisting of a finite number of replicas of the system, is constructed. These replicas can be generated by linear interpolation between the two end states. Every two adjacent replicas are connected by a spring, mimicking an elastic band made up of beads and springs. Beads in the band can be equally spaced in a relaxation process due to the spring forces. To solve the problems of corner cutting and sliding down that often arise with the plain elastic band method, a force projection is needed; this is what is referred to as the “nudging” operation [7]. With appropriate relaxation, the band converges to the MEP. Figure 12.1 illustrates the NEB method by showing an elastic band before and after relaxation on the energy contour of a model system with two degrees of freedom.

The algorithm of the NEB method involves the following basic steps. According to Henkelman *et al.* [9], let us denote  $\mathbf{R}_i$  as the atomic coordinates in the system at replica  $i$ . Given an estimate of the unit tangent to the path at each replica  $\mathbf{t}_i$ , the force on each replica contains the parallel component of the spring force and perpendicular component of the potential force:

$$\mathbf{F}_i = -\nabla E(\mathbf{R}_i)|_{\perp} + (\mathbf{F}_i^s \cdot \mathbf{t}_i)\mathbf{t}_i \quad (12.2)$$

where  $\nabla E(\mathbf{R}_i)$  is the gradient of the energy with respect to the atomic coordinates in the system at replica  $i$ ,  $\nabla E|_{\perp}$  is the component of the gradient perpendicular to  $\mathbf{t}_i$  and it can

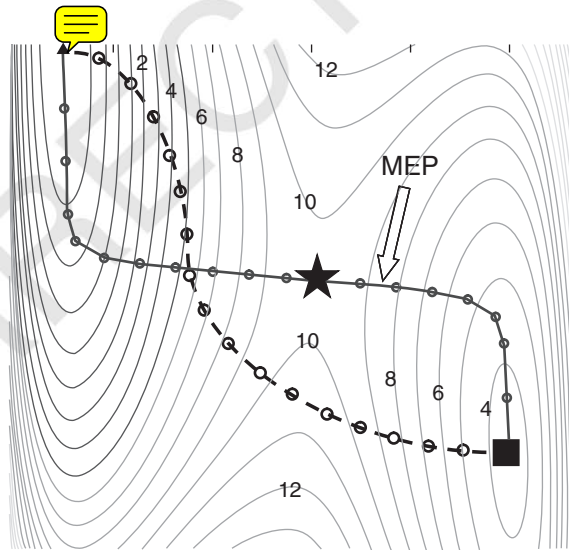


**Figure 12.1** An illustration of the NEB method by using the energy contour of a model system with two degrees of freedom. The dashed line represents an initially guessed MEP that links the initial (triangle) and final (square) states of local energy minima; the solid curve is the converged MEP passing through the saddle point (star)

be obtained by subtracting out the parallel component:

$$\nabla E(\mathbf{R}_i)|_{\perp} = \nabla E(\mathbf{R}_i) - [\nabla E(\mathbf{R}_i) \cdot \mathbf{t}_i] \mathbf{t}_i \quad (12.3)$$

In Equation (12.2),  $\mathbf{F}_i^s$  is the spring force acting on replica  $i$  and it can be evaluated according to

$$\mathbf{F}_i^s = k(|\mathbf{R}_{i+1} - \mathbf{R}_i| - |\mathbf{R}_i - \mathbf{R}_{i-1}|) \mathbf{t}_i \quad (12.4)$$

where  $k$  is the spring constant. Henkelman *et al.* [9] also discussed in detail how to estimate the tangent  $\mathbf{t}_i$ , minimize the force  $\mathbf{F}_i$ , and find the saddle point by the climbing image method, and so on.

The converged MEP is usually plotted as the energy, relative to the initial state, versus reaction coordinate. The latter can be defined in the following sense. Each replica on the MEP is a specific configuration in a  $3N$  configurational hyperspace, where  $N$  is the number of movable atoms in the simulation. For each replica one calculates the hyperspace arc length

$$l \equiv \int_{\mathbf{R}_0^{3N}}^{\mathbf{R}_i^{3N}} \sqrt{d\mathbf{R}^{3N} \cdot d\mathbf{R}^{3N}} \quad (12.5)$$

between the initial state  $\mathbf{R}_0^{3N}$  and the state of the replica  $\mathbf{R}_i^{3N}$ . The normalized reaction coordinate  $s$  can be calculated according to  $s = l/l_0$ , where  $l_0$  denotes the hyperspace arc length between the initial and final states.

### Example: Vacancy Migration in Cu

Let us consider the application of the NEB method to a simple problem of migration of a single vacancy in an otherwise perfect crystal of Cu. The system is initially a cube of face-centered-cubic (FCC) lattice with 500 atoms. The side length of the cube is  $5a_0$ , where  $a_0$  is the equilibrium lattice constant, 3.615 Å. A vacancy is generated by simply removing one atom from the perfect lattice. The vacant site in the initial (i) and final (f) configurations differs by a displacement of  $a_0/\sqrt{2}$  in the  $\langle 110 \rangle$  direction. Prior to the NEB calculation, both the initial and final configurations are fully relaxed to the zero stress under periodic boundary conditions, such that they correspond to two local energy minima on the zero-stress PES. The embedded atom potential (EAM) of Cu [14] is used in calculations.

Figure 12.2 shows the converged MEP from an NEB calculation, giving a vacancy migration barrier of 0.67 eV, consistent with experimental measurement of 0.71 eV [14]. The atomic configurations of the initial, saddle point, and final states are shown in Figure 12.2. Incidentally, the reaction coordinate in this case can be physically considered as the displacement of the vacancy (normalized by  $a_0/\sqrt{2}$ ) in the  $\langle 110 \rangle$  direction from the initial to final state, while it has been mathematically calculated according to the hyperspace arc length along the MEP (Equation (12.5)).

#### 12.2.2 The Free-End NEB Method

The NEB method is effective in finding the MEP of a highly localized activation process that involves the rearrangement of a small number of atoms, such as lattice and surface

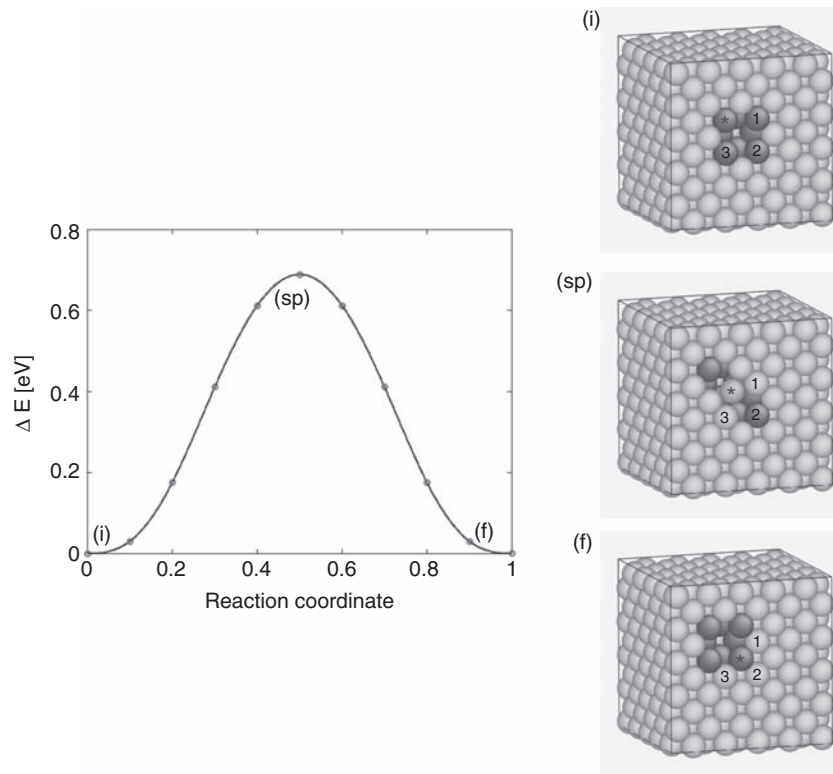


**Figure 12.2** MEP of migration of a single vacancy in an fcc Cu lattice. Also shown are the atomic configurations of the initial (i), saddle point (sp), and final (f) states. The migration of such a vacancy in the  $\langle 110 \rangle$  direction can be better visualized in terms of displacing an atom (adjacent to the vacant site) in the opposite direction; that is, the starred atom moving in between (i) and (f)

diffusion. However, it is inefficient to probe the activation process of extended three-dimensional (3D) defects such as dislocations and crack fronts, typically involving the collective motion of a large group of atoms and thus requiring a large model system with a long reaction path. This issue becomes more significant when the energy landscape is highly tilted by the applied load, such that the saddle point becomes closer to the initial state. Under such a condition, the plain NEB method becomes highly inefficient. That is, although only a small portion of the path close to the initial state is actually needed for finding the saddle point, a large number of replicas, and thus computations, have to be used to ensure the sufficient nodal densities for mapping out the long path between the saddle point and final state. To improve the computational efficiency, a free-end NEB method [15] has been developed.

The idea of the free-end NEB method is to reduce the modeled path length. This is realized by cutting short the elastic band and meanwhile allowing the end of the shortened band to move freely on an energy iso-surface close to the beginning of the band. The free-end NEB method contrasts with the plain one that requires the fixed final state at an

energy minimum far from the beginning. To appreciate the need for allowing the final state to move freely on an energy iso-surface, we note that if the initial state (node 0) is a local minimum and the final state (node  $n$ ) is not, but fixed during relaxation, then the NEB algorithm can behave badly. That is, node  $n - 1$  moves along its potential gradient except the component parallel to the path direction. If the fixed node  $n$  is not chosen to be right on the MEP, node  $n - 1$  will droop down and end up having much lower energy than node  $n$ . In the relaxation process it will drag all the path nodes along due to the spring force, which makes the quality of the NEB mesh degrades with time.

Consider, for example, a process of dislocation nucleation with the saddle-point energy of around 0.2 eV (taking the energy of node 0 zero). Usually, it would be sufficient if final node's energy is  $-0.3$  eV, since this means the final node is already in another attraction basin on the PES. Instead of seeking energy minimization, the free-end NEB algorithm requires that the final node's energy stays constant on the energy iso-surface of  $-0.3$  eV. As shown schematically in Figure 12.3a, the band swings to improve nodal density around the saddle point. Figure 12.3b shows a converged MEP from a model problem of a dislocation loop bowing out from a mode II crack tip, with the saddle-point configuration shown in Figure 12.3c. Here, the final state is fixed at 0.3 eV below the initial state. The free-end NEB method captures the saddle point with only seven replicas along the band, thus significantly improving the computational efficiency.

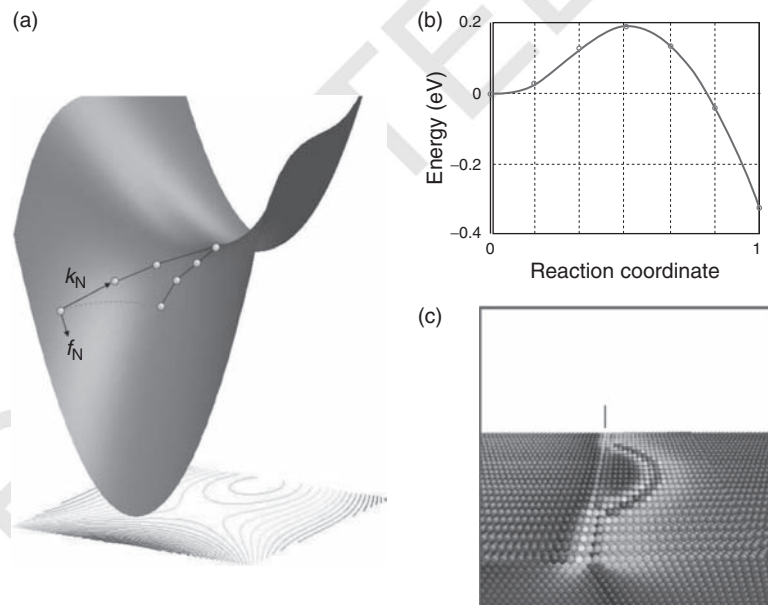


**Figure 12.3** The free-end NEB method enables an efficient reaction pathway calculation of extended defects in the large system. (a) Illustration of the method showing one end of the elastic band is fixed and the other is freely moved along an energy contour. (b) An example of the converged MEP from the free-end NEB method calculation; the end node is pinned at 0.3 eV below the initial state. (c) The corresponding saddle-point structure of a dislocation loop bowing out from a mode II crack tip (the upper half crystal is removed for clarity). Color version of this figure is available in the plate section

### 12.2.3 Stress-Dependent Activation Energy and Activation Volume

Increasing the applied stress will generally increase the thermodynamic driving force, reduce the energy barrier, and, accordingly, increase the rate of a thermally activated process [16]. Consider, for example, the nucleation of a dislocation loop from the surface of a Cu nanowire, Figure 12.4a. Suppose we begin to apply an axial stress  $\sigma$  in incremental steps. Initially, a dislocation would not form spontaneously because the driving force is not sufficient to overcome the nucleation resistance. What does this mean? Consider an initial configuration of a perfect wire and a final configuration with a fully nucleated partial dislocation; that is, states “i” and “f” in Figure 12.4b, respectively. At low loads (e.g.,  $\sigma_1 < \sigma_{cr}$  in Figure 12.4c), the initial configuration (white circle) has a lower energy than the final configuration (black circle). They are separated by an energy barrier (gray circle) with the saddle-point (sp) configuration shown in Figure 12.4b. At this load level, the nucleation is thermodynamically unfavorable because the energy of the final state is higher than the initial one. As the load increases, the system will be driven toward the final state, such that the nucleation becomes favorable thermodynamically when  $\sigma_2 > \sigma_{cr}$ . One can regard the overall energy landscape as being tilted toward the final state with a corresponding reduction in the energy barrier – compare the saddle-point states (gray circles) in Figure 12.4c. As the load increases further, the biasing becomes stronger. So long as the barrier remains finite, the state of a perfect wire will not move out of its initial basin without additional activation, such as from thermal fluctuations. When the load reaches the point where the nucleation barrier disappears altogether, the wire is then unstable at the initial configuration. It follows that a dislocation will nucleate instantaneously without any thermal activation. This is the athermal load threshold, denoted by  $\sigma_{ath}$  in Figure 12.4c.

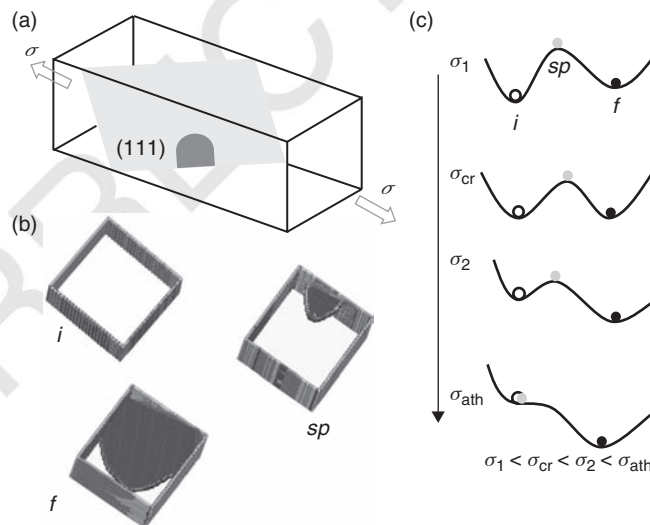


**Figure 12.4** Effects of the stress-dependent activation energy. (a) Schematic of surface dislocation nucleation in a nanowire at a given applied load. (b) Atomic structure of initial (i), saddle-point (sp) and final (f) states of surface nucleation. (c) Energy landscape at different applied loads; white circle represents the initial state (i), black circle is the final state (f), and gray circle corresponds to the saddle-point (sp) state in between

A concept related to the stress dependence of activation energy is activation volume, defined as

$$\Omega = -\frac{\partial Q(\sigma, T)}{\partial \sigma} \quad (12.6)$$

Physically, the activation volume corresponds to the amount of material (i.e., volume of atoms) in the high-energy state in a thermally activated process. As such, it measures the individualistic and collective nature of transition. During thermal activation, the stress does work on the activation volume to assist the transition by reducing the effective energy barrier. To reflect this stress-work effect, the rate formula of Equation (12.1) is commonly rewritten as

$$v = v_0 \exp\left(-\frac{Q_0 - \sigma\Omega}{k_B T}\right) \quad (12.7)$$

where  $Q_0$  is the activation energy at zero stress.

Different rate processes can have drastically different characteristic activation volumes; for example,  $\Omega \approx 0.1b^3$  for lattice diffusion versus  $\Omega \approx 1000b^3$  for the Orowan looping of a dislocation line across the pinning points in coarse-grained metals, where  $b$  is the Burgers vector length. As a result, the activation volume can serve as an effective kinetic signature of deformation mechanism. This is illustrated by the schematic in Figure 12.5, where the activation volume corresponds to the slope of an activation energy curve plotted as a function of stress. Notice that while the activation volume generally varies with stress, it is often treated as a constant when the rate or stress change is not large. Suppose the two competing processes have the same activation energy (indicated by the short-dash line in Figure 12.5) giving the same rate of transition, one can use the activation volume to identify the operative one in an experiment or a simulation. Furthermore, Figure 12.5 indicates that for the two processes with different activation volumes, the process with a higher energy barrier at low stresses may change to have a lower barrier at high stresses.

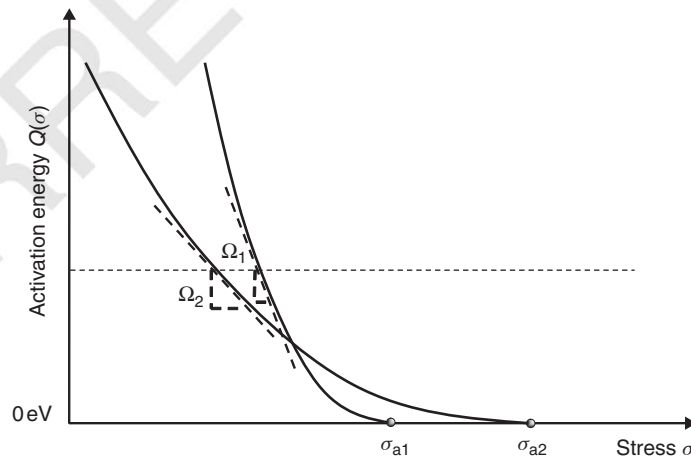


**Figure 12.5** Schematic of the stress-dependent activation energy for two competing thermally activated processes. They have different activation volumes ( $\Omega_1$  versus  $\Omega_2$ ) and athermal threshold stresses ( $\sigma_{a1}$  versus  $\sigma_{a2}$ )

This cross-over of energy barriers often underlies the switching of the rate-controlling mechanism in experiments.

In experiments, the activation volume can be determined by measuring the strain-rate sensitivity. Consider, as an example, uniaxial tension of a polycrystalline specimen. The empirical power-law relation is often used to represent the measured stress  $\sigma$  versus strain rate  $\dot{\epsilon}$  response:

$$\frac{\sigma}{\sigma_0} = \left( \frac{\dot{\epsilon}}{\dot{\epsilon}_0} \right)^m \quad (12.8)$$

where  $\sigma_0$  is the reference stress,  $\dot{\epsilon}_0$  is the reference strain rate, and  $m$  is the nondimensional rate-sensitivity index, which generally lies in between 0 and 1 ( $m=0$  gives the rate-independent limit and  $m=1$  corresponds to the linear Newtonian flow). The apparent activation volume  $\Omega^*$  is conventionally defined as

$$\Omega^* \equiv \sqrt{3} k_B T \frac{\partial \ln \dot{\epsilon}}{\partial \sigma} \quad (12.9)$$

Combining Equations (12.8) and (12.9), one can readily show that  $m$  is related to  $\Omega^*$  by [17]

$$m = \sqrt{3} \frac{k_B T}{\sigma \Omega^*} \quad (12.10)$$

In Equations (12.9) and (12.10), the factor of  $\sqrt{3}$  arises because, similar to the von Mises yield criterion, the normal stress  $\sigma$  is converted to the effective shear stress  $\tau^*$  according to  $\tau^* = \sigma/\sqrt{3}$ . Since  $\tau^*$  is related to the resolved shear stress on a single slip plane  $\tau$  by  $\tau^* = M/\sqrt{3}\tau$ , where  $M=3.1$  is the Taylor factor, it follows that the true activation volume  $\Omega$  associated with a unit process and the apparent activation volume  $\Omega^*$  measured from a polycrystalline sample are related by

$$\Omega^* = \frac{\sqrt{3}}{M} \Omega \quad (12.11)$$

The activation volume and rate sensitivity provide a direct link between experimentally measurable plastic flow characteristics and underlying deformation mechanisms. However, this link can be complicated by such important factors as mobile dislocation density and strain hardening [18].

Finally, we note that the scalar activation volume in Equations (12.6) and (12.7) can be generalized to a definition of the activation volume tensor [19], when all the stress components are considered. Albeit broad implications of the tensorial activation volume, in this chapter we focus on the simple scalar activation volume for highlighting its physical characteristics and usefulness. Importantly, the activation volume can be determined by both experiment and atomistic modeling, thus providing a unique link in coupling the two approaches for revealing the rate-controlling deformation mechanisms [15,17].

#### 12.2.4 Activation Entropy and Meyer–Neldel Compensation Rule

In order to provide a reasonable estimate of the absolute magnitude of the rate of a thermally activated process, one should also pay special attention to the effect of activation

entropy  $S(\sigma)$  [20–24]. The activation free energy  $Q(\sigma, T)$  in Equation (12.1) can be decomposed into

$$Q(\sigma, T) = E(\sigma) - TS(\sigma) \quad (12.12)$$

where  $E(\sigma)$  is the activation enthalpy that corresponds to the energy difference between the saddle point and initial equilibrium state on the 0 K PES. Substitution of Equation (12.12) into Equation (12.1) leads to

$$v = \tilde{v}_0 \exp\left(-\frac{E(\sigma)}{k_B T}\right) \quad (12.13)$$

where

$$\tilde{v}_0 = v_0 \exp\left(\frac{S(\sigma)}{k_B}\right) \quad (12.14)$$

It should be emphasized that the pre-exponential factor  $\tilde{v}_0$  in Equation (12.13) generally varies for different rate processes. More importantly,  $\tilde{v}_0$  changes for the same kind of processes under different applied stresses as well. As seen from Equation (12.14), such a change arises due to the change of activation entropy  $S(\sigma)$ . There is a well-known empirical Meyer–Neldel compensation law or iso-kinetic rule [25], which suggests that  $S(\sigma)$  is likely to correlate the activation energy by

$$S(\sigma) = \frac{E(\sigma)}{T_{MN}} \quad (12.15)$$

where  $T_{MN}$  denotes the Meyer–Neldel temperature constant.

The so-called “compensation” rule can be understood as follows: when the applied stress decreases at a constant temperature, the activation energy  $E(\sigma)$  typically increases (see Figure 12.5), causing a decrease of the value of  $\exp(-E(\sigma)/k_B T)$ . However, according to Equation (12.15), the activation entropy  $S(\sigma)$ , and accordingly  $\tilde{v}_0$ , will increase with  $E(\sigma)$ . As a result, the rate of activation  $v$  in Equation (12.13) does not decrease as rapidly as one would expect from only considering  $\exp(-E(\sigma)/k_B T)$ . According to Yelon *et al.* [26], the Meyer–Neldel compensation law is obeyed in a wide range of kinetic processes, including annealing phenomena, electronic processes in amorphous semiconductors, trapping in crystalline semiconductors, conductivity in ionic conductors, ageing of insulating polymers, biological death rates, and chemical reactions.

The empirical linear relation between the activation energy and activation entropy in Equation (12.15) is surprisingly simple and effective. Such a remarkable connection has been explained earlier in the context of solid-state diffusion, and more generally through the role of multi-excitation entropy [27,28]. Intuitively, the activation process with large activation energy involves the collective motion of a group of atoms. This gives rise to a large number of ways in which the activation can be done through the multi-phonon processes; namely, a large entropy change between the saddle point and initial equilibrium state. On the other hand, the increasing number of activated atoms is also manifested through the increase of activation volume  $\Omega$  defined by Equations (12.6) and (12.7).

Substitution of Equation (12.15) into Equation (12.12) gives

$$Q(\sigma, T) = E(\sigma) \left(1 - \frac{T}{T_{MN}}\right) \quad (12.16)$$

This relation furnishes a simple estimate, and interpretation, of the Meyer–Neldel temperature  $T_{MN}$ . Mott assumed  $T_{MN}$  to be the melting temperature of the crystal by noting that the activation free energy  $Q(\sigma, T)$  should approach zero at the melting temperature [20]. This provides an explanation of the large pre-factor of the temperature exponential in the measured rate of grain-boundary slip in pure polycrystalline aluminum. Generally,  $T_{MN}$  can be treated as the local melting or disordering temperature [21]. More extensive discussions on the activation entropy and Meyer–Neldel compensation rule can be found in a recent atomistic study of surface dislocation nucleation by Hara and Li [23].

### 12.3 Nanomechanics Case Studies

The NEB method has been applied successfully to a wide range of nanomechanics problems. In this section we present the case studies to clarify the concepts and demonstrate the applications. These cases are taken mostly from our own work. In Section 12.3.1, the crack-tip dislocation emission is discussed to demonstrate the necessity of 3D simulation of energy barriers as opposed to two-dimensional (2D) simulation. In Section 12.3.2, the stress-mediated chemical reaction is presented to illustrate the competing reaction pathways, mediated by stress. In Section 12.3.3, the dislocation and interface interaction is studied in nanotwinned Cu. This subsection highlights how to bridge the laboratory experiments with atomistic simulation of the rate-controlling mechanisms in terms of rate sensitivity and activation volume. In Section 12.3.4, surface dislocation nucleation in a nanowire is studied to predict the temperature and strain-rate dependence of strength limit and yield stress spanning a wide range of loading conditions. Finally, in Section 12.3.5 we present the size effects on fracture, with an emphasis on the difference of energy barriers under stress- versus strain-controlled loadings.

#### 12.3.1 Crack Tip Dislocation Emission

An important problem in the study of the mechanical behavior of materials is to understand the ductile–brittle transition of fracture. This has been studied in terms of competition between dislocation emission and cleavage bond breaking at an atomically sharp crack tip [29]. To evaluate the rate of dislocation emission from a crack tip, one needs to determine the saddle-point configuration and energy barrier of a dislocation loop nucleating from a crack tip. This has been studied by using various approaches, including the dislocation line model [29], the semi-analytic model based on the Peierls concept (i.e., periodic relation between shear stress and atomic shear displacement) [30], and the numerical approach of the boundary integral [31]. Application of the NEB method to this problem makes possible a direct atomistic determination of the saddle-point configuration and energy barrier of dislocation nucleation [32].

Consider, as an example, a crack in an FCC single crystal of Cu. The simulation cell consists of a cracked cylinder cut from the crack tip, with radius  $R = 80 \text{ \AA}$ . The straight crack front, lying on a (111) plane, runs along the [110] direction. The cracked system is subjected to a mode I load of the stress intensity factor  $K_I = 0.44 \text{ MPa m}^{1/2}$ . Atoms within  $5 \text{ \AA}$  of the outer surface are fixed according to a prescribed atomic displacement, and all the other atoms are fully relaxed. The embedded atom (EAM) potential of Cu is

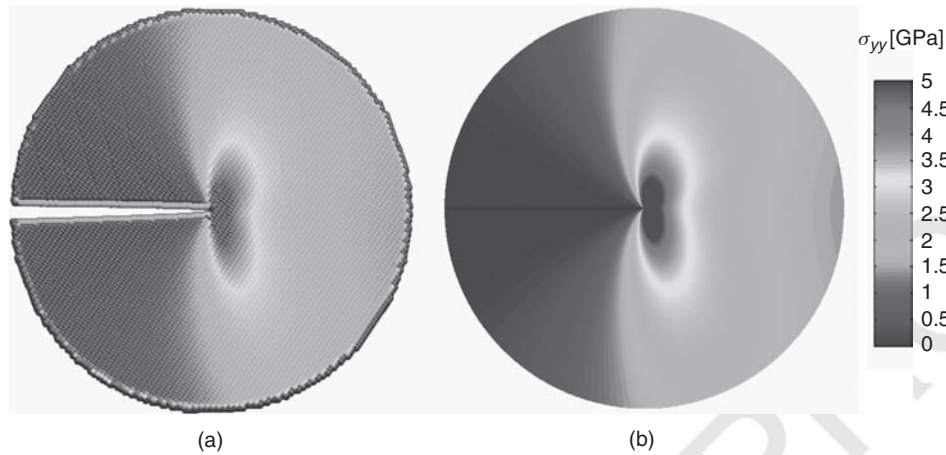


**Figure 12.6** Distribution of stress  $\sigma_{yy}$  near a crack tip in Cu, subjected to an applied stress intensity factor  $K_I = 0.44 \text{ MPa m}^{1/2}$  [32]. (a) Atomistic result from energy minimization of a cracked lattice and the atomic stress is calculated by the virial formula. (b) Numerical result based on the analytic solution of the crack-tip stress field from continuum fracture mechanics

used in calculations. To validate the atomistic study, we obtained the consistent atomic calculation (Figure 12.6a) and analytic solution (Figure 12.6b) of the stress distribution near the crack tip.

It should be emphasized that the thermally activated dislocation emission is intrinsically a 3D process involving the growth of a small dislocation loop from the crack front. In other words, one cannot simply use a quasi-2D NEB calculation to determine the energy barrier of emission of a straight line parallel to the crack front, which will increase unphysically with thickness of the simulation cell. Figure 12.7a shows the schematics of emission of a 3D dislocation loop on a  $\{111\}$  slip plane inclined to the crack tip. In the NEB calculation, the initial state is the loaded crack system without dislocation, and the final state consists of a fully nucleated dislocation. Note that the atomic structure of the initial state corresponds to that in Figure 12.6, but replicated by 24 unit cells with a total length of  $61 \text{ \AA}$  in the out-of-plane direction, along which a periodic boundary condition is imposed. Such a large thickness minimizes the interaction of a dislocation loop between neighboring supercells in the out-of-plane direction. The final state can be generated by a two-step operation: first, impose a high load to nucleate a dislocation instantaneously; second, unload the system by prescribing the same atomic positions of boundary atoms as the initial state and then relax the system.

The converged MEP from the NEB calculation is shown in Figure 12.7b, giving an energy barrier of  $1.1 \text{ eV}$ . Figure 12.7c shows the saddle-point atomic configuration of an emanating dislocation loop. From this structure, the shear displacement distribution on the slip plane is quantitatively extracted as shown in Figure 12.7d, which clearly demonstrates that the dislocation line is the boundary between slipped (red) and unslipped (blue) regions. The implications of those results on homogeneous versus heterogeneous dislocation nucleation at the crack tip are discussed by Zhu *et al.* [32].

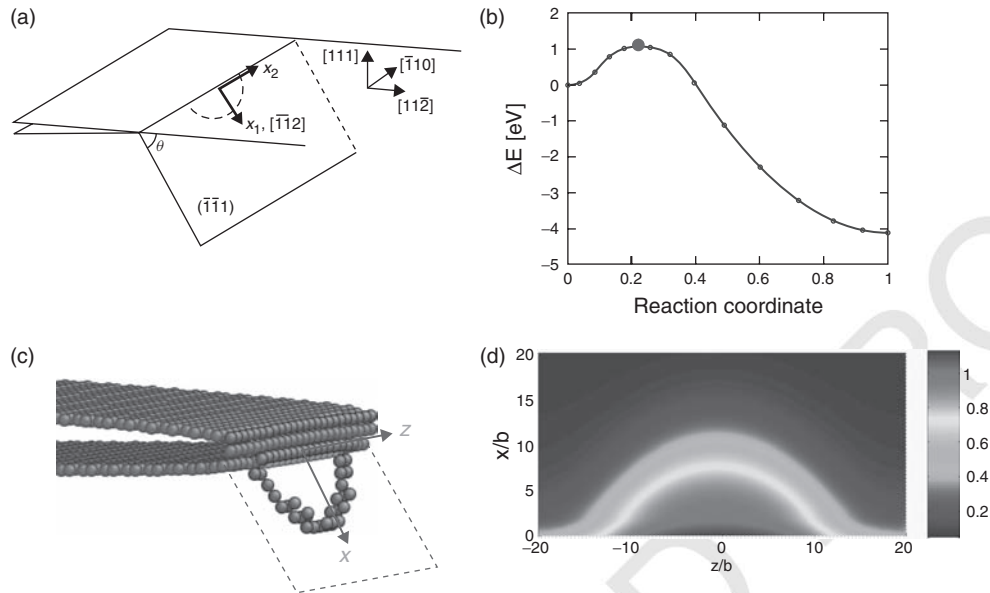


**Figure 12.7** The NEB calculation of dislocation emission from a crack tip in single-crystal Cu [32]. (a) Orientations of the crack and the inclined  $\{111\}$  slip plane across which a dislocation loop nucleates. (b) MEP of emission of a 3D dislocation loop. (c) Saddle-point atomic structure. Atom color indicates coordination number, and atoms with perfect coordination ( $N = 12$ ) are made invisible. (d) Contour plot of shear displacement distribution, normalized by the Burgers vector length  $b = 1.476 \text{ \AA}$ , across the slip plane; this plot is extracted from (c)

### 12.3.2 Stress-Mediated Chemical Reactions

Chemical reaction rates in solids are known to depend on mechanical stress levels. This effect can be generally described in terms of a change of activation energy barrier in the presence of stress. A typical example is stress corrosion of silica ( $\text{SiO}_2$ ) glass by water; the strength of the glass decreases with time when subjected to a static load in an aqueous environment [33]. The phenomenon, also known as delayed failure or static fatigue, essentially refers to the slow growth of pre-existing surface flaws as a result of corrosion by water in the environment. From a microscopic viewpoint, it is believed that the intrusive water molecules chemically attack the strained siloxane ( $\text{Si-O-Si}$ ) bonds at the crack tip, causing bond rupture and formation of terminal silanol ( $\text{Si-OH}$ ) groups which repel each other at the conclusion of the process [34]. This molecular-level mechanism, intrinsically, governs the macroscopic kinetics of quasi-static crack motion.

Stress corrosion of silica by water is studied by exploring the stress-dependent PES computed at the level of molecular orbital theory [35]. Figure 12.8a shows that an ordered silica nanorod with clearly defined nominal tensile stress is constructed to model a structural unit of the stressed crack tip. Using the NEB method, we are able to explicitly map out families of reaction pathways, parameterized by the continuous nominal stress. Figure 12.8b shows that three competing hydrolysis reaction pathways are determined, each involving

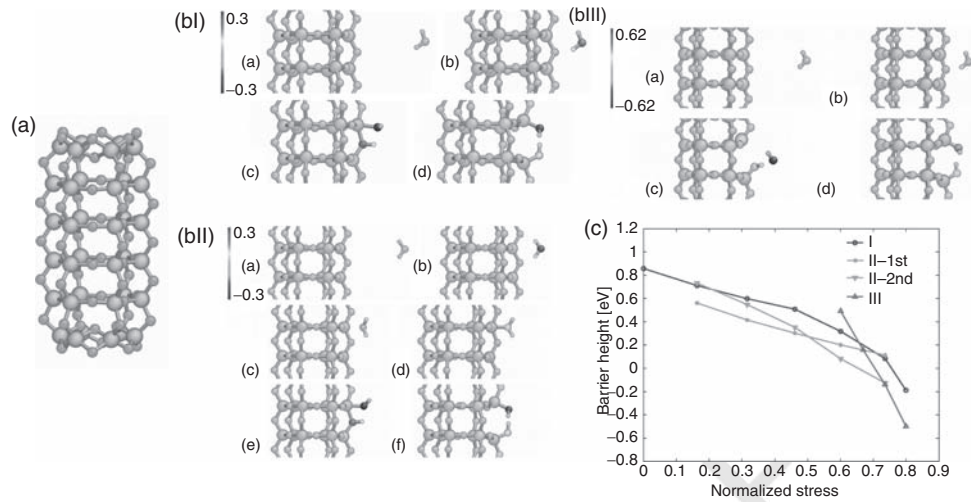


**Figure 12.8** Stress-dependent molecular reaction pathways between an SiO<sub>2</sub> nanorod and a single water molecule [35]. (a) Structure of a fully relaxed SiO<sub>2</sub> nanorod. (b) MEPs of reactions, involving the characteristic initiation step: (I) water dissociation, (II) molecular chemisorption, and (III) direct siloxane bond rupture. Atoms are colored by charge variation relative to the initial configuration. (c) Comparison of the stress-dependent activation barriers for the three molecular mechanisms of hydrolysis

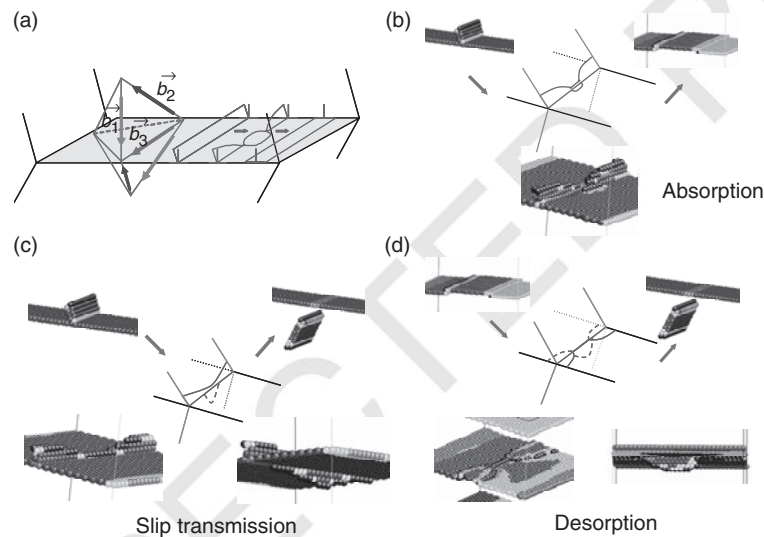
a distinct initiation step: (I) water dissociation, (II) molecular chemisorption, and (III) direct siloxane bond rupture.

Figure 12.8c compares the energy barriers as a function of stress for the three different mechanisms of hydrolysis reaction. Evidently, the tensile stress will reduce the activation energy barrier for any specific reaction mechanism. More importantly, as the relative barrier height of different mechanisms changes with an increase of stress, the switching of rate-limiting steps will occur either within one type of reaction pathway (e.g., the second reaction mechanism) or among different reaction mechanisms. The three reactions dominate at low, intermediate, and high stress levels, respectively.

### 12.3.3 Bridging Modeling with Experiment

As an important type of nanostructured metal, ultrafine crystalline Cu with nanoscale growth twins has attracted considerable attention in recent years. Experiments by Lu *et al.* [36] showed that nano-twinned Cu exhibited an unusual combination of ultrahigh strength and reasonably good tensile ductility, while most nanostructured metals have high strength and low ductility. As an essential step toward understanding the mechanistic origins of such extraordinary mechanical properties, the experiment showed that the nano-twinned Cu increases the rate sensitivity ( $m \approx 0.02$ ) by up to an order of magnitude relative to microcrystalline metals with grain size in the micrometer range, and a concomitant decrease in the activation volume by two orders of magnitude (e.g., down to  $\Omega \approx 20b^3$  when twin lamellae are approximately 20 nm thick) [37].

We have studied the mechanistic origin of decreased activation volume and increased rate sensitivity in the nano-twinned system [15]. Slip transfer reactions are simulated between a lattice dislocation and a coherent twin boundary (TB), involving dislocation absorption and desorption into the TB and slip transmission across the TB. The dislocation–interface reactions have previously been studied by MD simulations [38]. To overcome the well-known time-scale limitation of molecular dynamics, the free-end NEB method is used to determine the MEPs of the above-mentioned slip transfer reactions (Figure 12.9), such that atomistic predictions of yield stress, activation volume, and rate sensitivity can be directly compared with measurements from laboratory experiments on long time scales (seconds to minutes); see Table 12.1. The modeling predictions are consistent with experimental measurements, thereby showing that the slip transfer reactions are the rate-controlling mechanisms in nano-twinned Cu.



**Figure 12.9** The free-end NEB modeling of twin-boundary-mediated slip transfer reactions [15]. (a) Schematics of dislocation–interface reactions based on double Thompson tetrahedra, showing different combinations of incoming and outgoing dislocations (the Burgers vectors with the same color) at a coherent TB. Atomic structures of the initial, saddle-point, and final states are shown for the slip transfer reactions, including (b) absorption, (c) direct transmission, and (d) desorption. Color version of this figure is available in the plate section

**Table 12.1** The free-end NEB calculations predict activation energy, activation volume, and yield stress for nano-twinned Cu, consistent with experimental measurements [15]

	Athermal stress threshold $\sigma_{\text{ath}}$	Activation volume $v^*$	Strain-rate sensitivity $m$
Uniaxial tension experiment	$\sim 1$ GPa		
Nanoindentation experiment	$> 700$ MPa	$12-22b^3$	$0.025-0.036$
Atomistic calculation	$780$ MPa	$24-44b^3$	$0.013-0.023$

### 12.3.4 Temperature and Strain-Rate Dependence of Dislocation Nucleation

Direct MD simulations have been widely used to explore the temperature and strain-rate dependence of defect nucleation. However, MD is limited to exceedingly high stresses and strain rates. To overcome this limitation, the statistical models have been developed that integrate transition-state theoretical analysis and reaction pathway modeling [21,24]. Such models require the atomistic input of the stress-dependent energy barriers of defect nucleation, which can be calculated by using the NEB method.

Consider, as an example, surface nucleation in a Cu nanopillar (Figure 12.10a) under a constant applied strain rate. Because of the probabilistic nature of the thermally activated nucleation processes, the nucleation stress has a distribution even if identical samples are used. The most probable nucleation stress is defined by the peak of the frequency distribution of nucleation events. Specifically, the statistical distribution of nucleation events is the product of a nucleation rate that increases in time and a likelihood of pillar

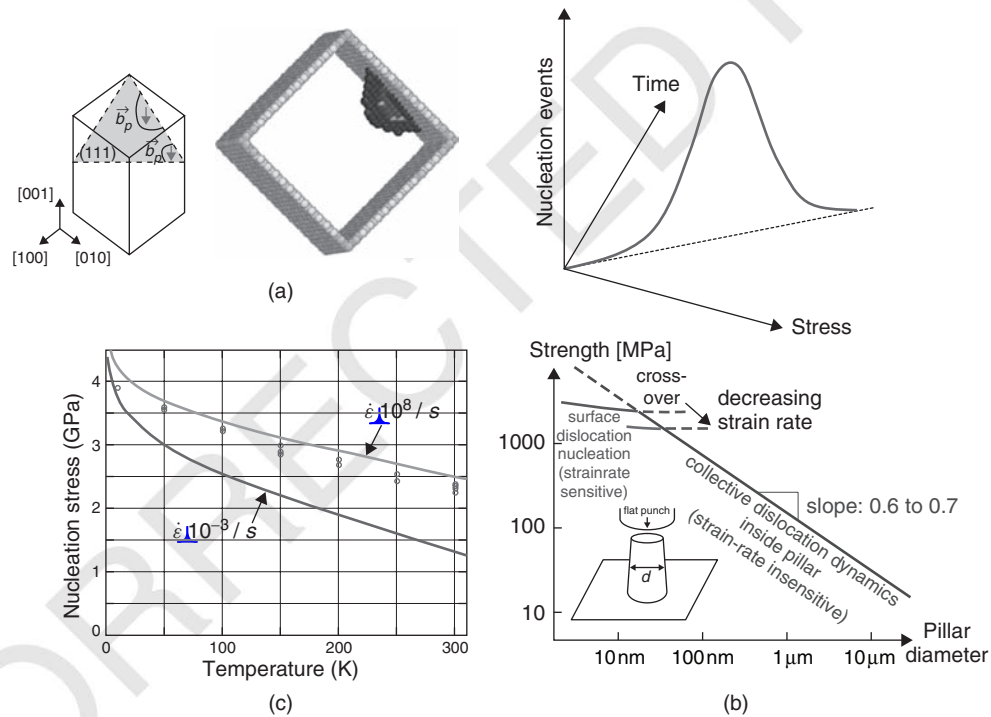


**Figure 12.10** Temperature and strain-rate dependence of surface dislocation nucleation [21]. (a) Nucleation of a partial dislocation from the side surface of a single-crystal Cu nanowire under uniaxial compression. (b) Under a constant strain rate, a peak of nucleation events arises because of the two competing effects: the increasing nucleation rate with time (stress) and decreasing survival probability without nucleation. (c) Nucleation stress as a function of temperature and strain rate from predictions (solid lines) and direct MD simulations (circles). (d) Illustration of the surface effect on the rate-controlling process and the size dependence of yield strength in micro- and nano-pillars of diameter  $d$  under compression

survival without nucleation that decreases with time. These two competing effects lead to a maximum at a specific time (stress), as illustrated in Figure 12.10b. The nucleation stress, therefore, represents the most likely moment of nucleation under a particular loading rate. It is not a constant.

Based on the above nucleation statistics-based definition, we have developed a nonlinear theory of the most probable nucleation stress as a function of temperature and strain rate. Here, the nonlinearity arises primarily because of the nonlinear stress dependence of activation energy, which has been numerically determined using the NEB calculations [21]. A key result from these calculations is that the activation volumes associated with a surface dislocation source are in a characteristic range of  $1-10b^3$ , which is much lower than that of the bulk dislocation processes ( $100-1000b^3$ ). The physical effect of such small activation volumes can be clearly seen from a simplified linear version of the theory, giving an analytic formula of the nucleation stress:

$$\sigma = \sigma_a - \frac{k_B T}{\Omega} \ln \frac{k_B T N v_0}{E \dot{\epsilon} \Omega} \quad (12.17)$$

where  $\sigma_a$  is the athermal stress of instantaneous nucleation,  $E$  is Young's modulus, and  $N$  is the number of equivalent nucleation sites on the surface. Notice that the nucleation stress  $\sigma$  has a temperature scaling of  $T \ln T$ , and the activation volume  $\Omega$  appears outside the logarithm, such that a small  $\Omega$  associated with a surface source should lead to sensitive temperature and strain-rate dependence of nucleation stress, as quantitatively shown in atomistic simulations; see Figure 12.10c. In nano-sized volumes, surface dislocation nucleation is expected to dominate, as supported by recent experiment. As shown schematically in Figure 12.10d, the strength mediated by surface nucleation should provide an upper bound to the size-strength relation in nanopillar compression experiments. This upper bound is strain-rate sensitive because of the small activation volume of surface nucleation at ultra-high stresses.

### 12.3.5 Size and Loading Effects on Fracture

In the study of brittle fracture at the nanometer scale, questions often arise:

1. Is the classical theory of Griffith's fracture still applicable?
2. What is the influence of the discreteness of the atomic lattice?
3. Do the stress- and strain-controlled loadings make a difference?

These questions can be directly addressed by the NEB calculations of energetics of nano-sized cracks [39].

Recall that, in the Griffith theory of fracture [40], one considers a large body with a central crack of length  $2a$ ; see Figure 12.11a, for example. Suppose the system is subject to an average tensile stress  $\sigma$ . This load can be imposed by either a fixed displacement or a constant force at the far field. Relative to the uncracked body under the same load (e.g., fixed displacement), the elastic energy decrease due to the formation of a crack of length  $2a$  is  $\pi\sigma^2 a^2/E$  per unit thickness (where  $E$  is Young's modulus) and the corresponding increase of surface energy is  $4\gamma a$ , where  $\gamma$  is the surface energy density. As a result, the total energy change is  $U(a) = 4\gamma a - \pi\sigma^2 a^2/E$ . The critical crack length of Griffith

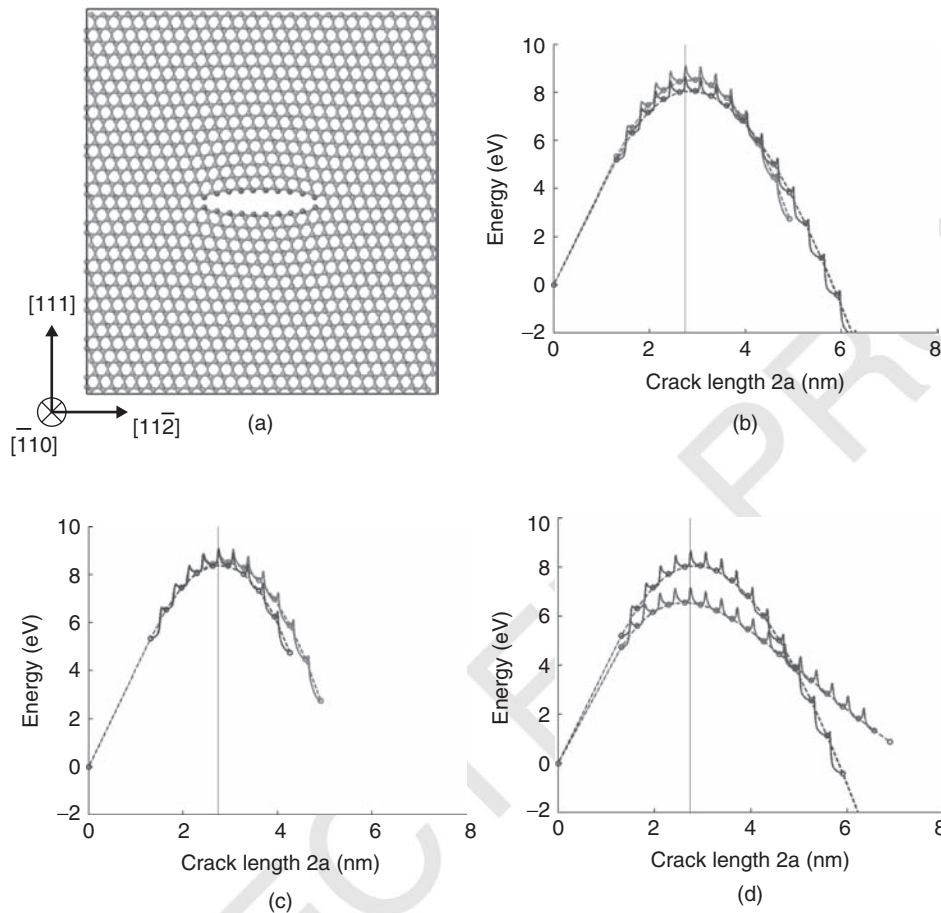


**Figure 12.11** Size and loading effects on nanoscale fracture in single-crystal Si [39]. (a) Relaxed atomic structure with a central nanocrack at its critical length of Griffith fracture,  $2a_{\text{cr}} = 3$  nm; the size of simulation cell is  $9.1 \times 10.1$  nm<sup>2</sup>. (b) The system's energy as a function of crack length under stress-controlled (red) and strain-controlled (blue) loading conditions; the size of simulation cell is  $18.3 \times 20.1$  nm<sup>2</sup>, doubling the width and height of the cell shown (a). (c) Sample-size effect on system's energy for stress-controlled fracture, showing the energy of the crack system in the cells of  $18.3 \times 20.1$  nm<sup>2</sup> (red) and  $9.1 \times 10.1$  nm<sup>2</sup> (brown). (d) Sample-size effect on system's energy for strain-controlled fracture, showing the energy of the crack system in the cells of  $18.3 \times 20.1$  nm<sup>2</sup> (blue) and  $9.1 \times 10.1$  nm<sup>2</sup> (green). Reprinted with permission from [39]. Copyright 2009 Elsevier

fracture  $2a_{\text{cr}}$  is defined in terms of the condition when  $U(a)$  reaches the maximum, giving  $a_{\text{cr}} = 2\gamma E / (\pi \sigma^2)$ . Note that the displacement/strain-controlled and force/stress-controlled loadings give the same formula of  $U(a)$  and  $a_{\text{cr}}$  in the classical fracture theory.

Figure 12.11b shows the atomistic calculations of  $U(a)$  for single-crystal Si based on the Stillinger–Weber (SW) interatomic potential [41]. In the figure, a circle represents the energy of a metastable state with a nominal crack length  $2a$  given by the number of broken bonds times the lattice spacing. The envelope curves connecting circles give  $U(a)$  under

stress-controlled (red) and strain-controlled (blue) loadings. The Griffith crack length can be determined by the maximum of  $U(a)$ , giving  $2a_{\text{cr}} = 2.8$  nm. Alternatively, one can evaluate the Griffith crack length using the material constants of  $E$  and  $\gamma$  calculated from the SW potential, giving  $2a_{\text{cr}} = 2.74$  nm, as indicated by vertical lines in Figure 12.11b–d. The agreement between the two methods for predicting the critical crack length (with a difference of less than one atomic spacing of 0.33 nm) suggests that the Griffith formula is applicable to the nanoscale fracture.

Energy barriers of crack extension arise because of the lattice discreteness, leading to the so-called lattice trapping effect [42]. In Figure 12.11b, each spike-like curve linking adjacent circles gives the MEP of breaking a single bond at the crack tip; that is, unit crack extension by one lattice spacing. The maximum of each MEP gives the energy barrier of bond breaking. Such MEPs manifest the corrugation of the atomic-scale energy landscape of the system due to the lattice discreteness. As a result, a crack can be locally “trapped” in a series of metastable states with different crack lengths and crack-tip atomic structures. The time-dependent kinetic crack extension then corresponds to the transition of the system from one state to another via thermal activation.

Figure 12.11 also demonstrates the effects of system size and loading method on the nanoscale brittle fractures. It is seen from Figure 12.11b that, when the system size is about 10 times larger than the crack size, the curves of  $U(a)$  are close for stress-controlled (red) and strain-controlled (blue) fracture. Comparison of Figure 12.11c and d indicates that  $U(a)$  for strain-controlled fracture is much more sensitive to the reduction of system size than the stress-controlled fracture. This is because the average stress in a sample under strain control can significantly change with crack length in small systems (i.e., the sample size is less than 10 times the crack length).

## 12.4 A Perspective on Microstructure Evolution at Long Times

A longstanding and still largely unresolved question in multiscale materials modeling and simulation is the connection between atomic-level deformation processes at the nanoscale and the overall system behavior seen on macroscopic time scales. Two special cases have been examined recently that may serve to elaborate on this issue [10]. One is the viscous relaxation in glassy liquids, where the shear viscosity increases sharply with supercooling. This is a phenomenon of temperature-dependent stress fluctuations, which is becoming amenable to atomistic simulations due to the development of a method for sampling microstructure evolutions at long times [43–45]. The other case is the slow structural deformation in solids, the phenomenon of anelastic stress relaxation and defect dynamics [46]. Although physically quite different, both problems involve microstructure developments that span many unit processes. The corresponding **MEPs** in these problems may be called TSP trajectories [43], to distinguish them from the **reaction pathways** discussed in Sections 12.2 and 12.3. In this chapter we have seen several atomistic studies where NEB is applicable, in which case one can evolve the system using transition-state theory and a knowledge of the activation energy of a particular transition. Since the traditional NEB method requires knowing the initial and final states of a reaction, tracking the system evolution over an extended time interval will require extension of the NEB methodology.

The search for an atomistic method capable of reaching the macro time scale has motivated the development of a number of simulation techniques, among them being

replace "MEPs" by  
"trajectories"  
replace "reaction  
pathways" by "MEPs"

hyperdynamics [47] and metadynamics [48,49], which are methods designed to accelerate the sampling of rare events. By the use of history-dependent bias potentials, metadynamics can enable the efficient sampling of the potential-energy landscapes, leading to the determination of the activation barriers and the associated rate constants through the transition-state theory. Here, we will briefly mention a metadynamics-based method which seems to be promising in dealing with deformation and reaction problems in nanomechanics.

### 12.4.1 Sampling TSP Trajectories

A procedure has recently been implemented that was designed to simulate situations where the system is trapped in a deep local minimum and, therefore, requires long times to get out of the minimum and continue exploration of the phase space [43]. The idea is to lift a system of particles out of an arbitrary potential well by a series of activation–relaxation steps. The algorithm is an adaptation of the metadynamics method originally devised to drive a system from its free-energy minima [48,49]. The particular procedure of activation–relaxation will be described here only schematically; for details, the reader should consult the original work [43].

Suppose our system starts out at a local energy minimum  $E_1^m$ , as shown in Figure 12.12a. To push the system out of its initial position a penalty function is imposed and the system is allowed to relax and settle into a new configuration (Figure 12.12b). The two-step process of activation and relaxation is repeated until the system moves to an adjacent local minimum, indicated in Figure 12.12c. As the process continues, the previous local minima are not visited because the penalty functions providing the

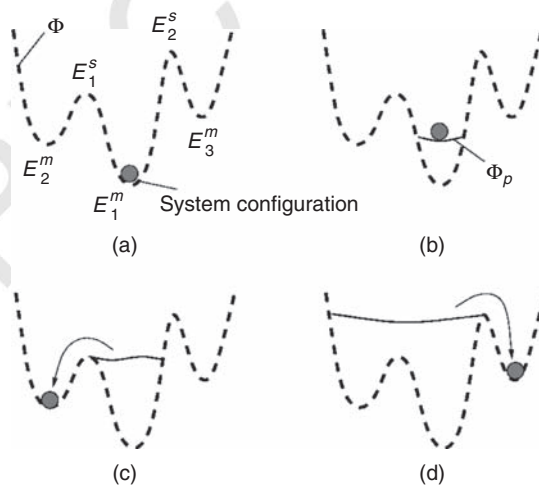


**Figure 12.12** Schematic illustration explaining the autonomous basin climbing (ABC) method [43]. Dashed and solid lines indicate original PES and penalty potential, respectively. Penalty functions push the system out of a local minimum to a neighboring minimum by crossing the lowest saddle barrier. Reprinted with permission from [43]. Copyright 2009 American Institute of Physics

previous activations are not removed; the system is, therefore, encouraged always to sample new local minima, illustrated in Figure 12.12d. The sequence of starting from an initial local minimum  $E_1^m$  to cross a saddle point  $E_1^s$  to reach a nearby local minimum  $E_2^m$ , and so on, thus generates a TSP trajectory; an example of three local minima and two saddle points is depicted in Figure 12.12. We will refer to this algorithm as the autonomous barrier climbing (ABC) method. The most distinguishing feature of metadynamics is the way in which the bias potential is formulated. The bias potential is history dependent, in that it depends on the previous part of the trajectory that has been sampled [48,49].

#### 12.4.2 Nanomechanics in Problems of Materials Ageing

We have recently started to explore how ABC could be used to provide an atomic-level explanation of mechanical behavior of materials governed by very slow microstructure evolution, involving time scales well beyond the reach of traditional atomistic methods [10]. Two problems were studied; one has to do with the temperature variation of the shear viscosity of glassy liquids [43–45] and the other concerns the relaxation behavior in solids undergoing creep deformation [46]. We believe there are other complex materials behavior problems where the understanding of long-time systems behavior may benefit from sampling of microscale processes of molecular rearrangements and collective interactions. As examples of a class of phenomena that could be broadly classified as materials ageing, we briefly introduce here an analogy between viscous flow and creep on the one hand and stress-corrosion cracking (SCC) and cement setting on the other hand [10]. All are challenges for atomistic modeling and simulation studies.

Figure 12.13 shows four selected functional behaviors of materials: temperature variation of viscosity of supercooled liquids, stress variation of creep strain rate in steel, stress variation of crack speed in a glass, and time variation of the shear modulus of a cement paste. Each is a technologically important characteristic of materials noted for slow microstructure evolution. It is admittedly uncommon to bring them together to suggest a common issue in sampling slow dynamics. Qualitatively speaking, these problems illustrate the possible extensions of the case studies that have been discussed in Section 12.3.

To bring out the commonality among the apparently different physical behaviors in Figure 12.13, we first note the similar appearance between Figure 12.13a and b, where the data are plotted against inverse temperature and stress, respectively. The presence of two distinct stages of variation may be taken to indicate two competing atomic-level responses. In the viscosity case we know the high- $T$  regime of small  $\eta$  and the low- $T$  stage of large  $\eta$  are governed by continuous collision dynamics and barrier hopping, respectively. One may expect analogous interplay between dynamical processes occurring at different spatial and temporal scales in the case of stress-driven creep. The variation of strain rate with stress and temperature, seen in Figure 12.13b, is a conventional way to characterize structural deformation.

The two stages are a low-stress strain rate, usually analyzed as a power-law exponent, and a high-stress high strain-rate regime. Attempts to explain creep on the basis of an atomic-level mechanism of dislocation climb are in its infancy [53]; the usefulness of TSP

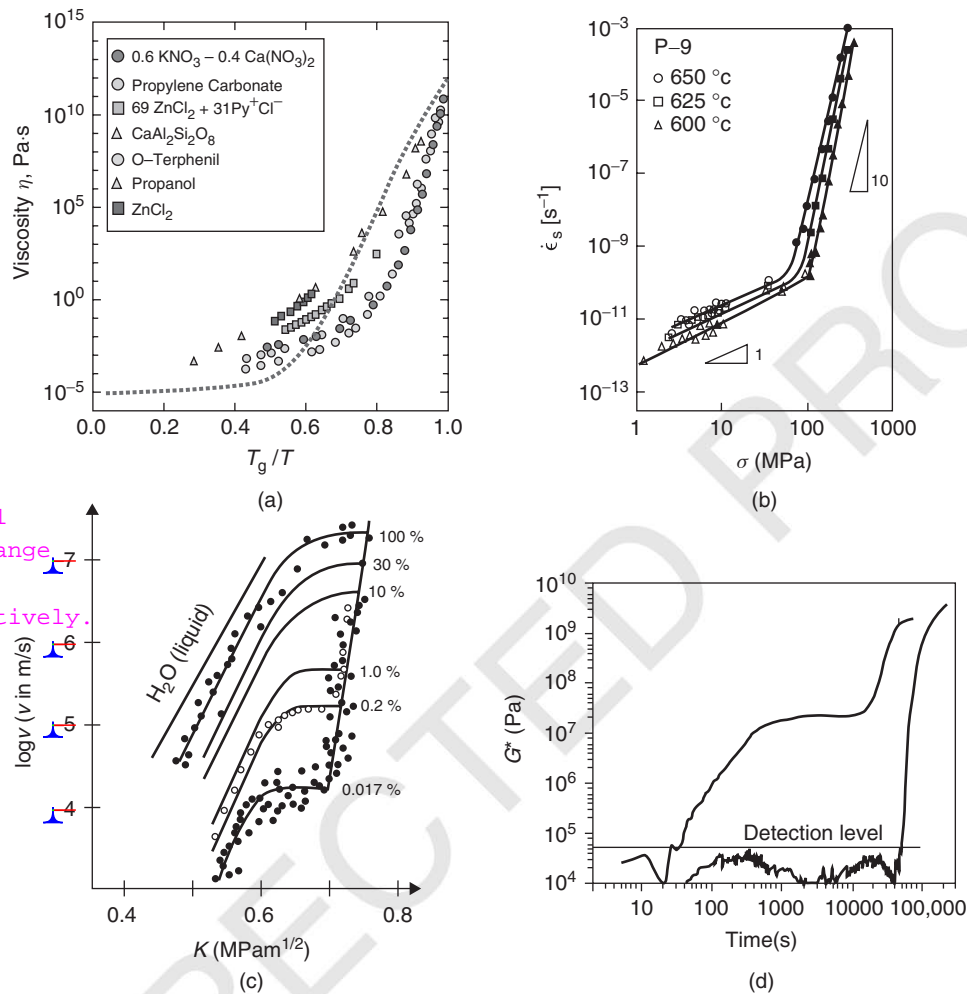


**Figure 12.13** A collection of materials' behaviors illustrating the defining character of slow dynamics. (a) Temperature variation of shear viscosity of supercooled liquids [50]. Reprinted with permission from [56]. Copyright 1988 Elsevier; (b) stress variation of strain rate in P-91 steel [51]. Reprinted with permission from [57]. Copyright 2005 Maney Publishing; (c) stress loading variation of crack speed in soda-lime (NaOH) glass at various humidities [33]. Reprinted with permission from [33]. Copyright 1967 Wiley; (d) time variation of shear modulus in hardening of Portland cement paste (water/cement ratio of 0.8) measured by ultrasound propagation [52]. Reprinted with permission from [58]. Copyright 2004 EDP Sciences

methods such as ABC is suggested by recent studies of self-interstitial [54] and vacancy clusters [55].

Viscosity and creep are phenomena where the system microstructure evolves through cooperative rearrangements or lattice defect interactions without chemical (compositional or stoichiometric) changes. In contrast, the stress variation of the crack velocity in

Figure 12.13c shows the classic three-stage behavior of SCC [56]. One can distinguish in the data a corrosion-dominated regime at low stress (stage I), followed by a plateau (stage II) where the crack maintains its velocity with increasing stress, and the onset of a rapid rise at high stress (stage III) where stress effects now dominate. Relative to Figure 12.13a and b, the implication here is that a complete understanding of SCC requires an approach where chemistry (corrosion) and stress effects are treated on an equal footing. This is an extension of the case study discussed in Section 12.3.2. The extension of ABC to reactions involving bond breaking and formation, which have been previously studied by MD simulation, is an area for further work.

Another reason we have for showing the different behaviors together in Figure 12.13 is to draw attention to a progression of microstructure evolution complexity, from viscosity to creep, to SCC, and to cement setting. In Figure 12.13d one sees another classic three-stage behavior in the hardening of cement paste [52]. The hydration or setting curve is known to everyone in the cement science community; on the other hand, an explanation in terms of molecular mechanisms remains elusive. A microstructure model of calcium silicate hydrate, the binder phase of cement, has recently been established [57] which could serve as starting point for the study of viscosity, creep deformation, and even the setting characteristics of cement. If viscosity or glassy dynamics is the beginning of this progression where the challenge lies in the area of statistical mechanics, followed by creep in the area of solid mechanics (mechanics of materials), then SCC and cement setting may be regarded as future challenges in the emerging area of chemo-mechanics.

Our brief outlook on viscous relaxation and creep deformation points to a direction for extending reaction pathway sampling to flow and deformation of matter in chemical and biomolecule applications. It seems to us that the issues of materials ageing and degradation in extreme environments should have fundamental commonality across a spectrum of physical and biological systems. Thus, one can expect that simulation-based concepts and algorithms allowing one to understand temporal evolution at the systems level in terms of molecular interactions and cooperativity will have enduring interest.

## References

- [1] Li, J. (2007) The mechanics and physics of defect nucleation. *MRS Bulletin*, **32**, 151–159.
- [2] Zhu, T., Li, J., Ogata, S., and Yip, S. (2009) Mechanics of ultra-strength materials. *MRS Bulletin*, **34**, 167–172.
- [3] Zhu, T. and Li, J. (2010) Ultra-strength materials. *Progress in Materials Science*, **55**, 710–757.
- [4] Yip, S. (2003) Synergistic science. *Nature Materials*, **2**, 3–5.
- [5] Yip, S. (2005) *Handbook of Materials Modeling*, Springer, Berlin.
- [6] Yip, S. (2010) Multiscale materials, in *Multiscale Methods* (ed. J. Fish), Oxford University Press, New York, pp. 481–511.
- [7] Jonsson, H., Mills, G., and Jacobsen, K.W. (1998) Nudged elastic band method for finding minimum energy paths of transitions, in *Classical and Quantum Dynamics in Condensed Phase Simulations* (eds. B.J. Berne, G. Ciccotti, and D.F. Coker), World Scientific, pp. 385–404.
- [8] Henkelman, G., Uberuaga, B.P., and Jonsson, H. (2000) A climbing image nudged elastic band method for finding saddle points and minimum energy paths. *Journal of Chemical Physics*, **113**, 9901–9904.
- [9] Henkelman, G., Johansson, G., and Jonsson, H. (2000) Methods for finding saddle points and minimum energy paths, in *Progress on Theoretical Chemistry and Physics* (ed. S.D. Schwartz), Kluwer Academic, pp. 269–300.
- [10] Kushima, A., Eapen, J., Li, J. *et al.* (2011) Time scale bridging in atomistic simulation of slow dynamics: viscous relaxation and defect mobility. *European Physical Journal B*, **82**, 271–293.

- [11] Voter, A.F., Montalenti, F., and Germann, T.C. (2002) Extending the time scale in atomistic simulation of materials. *Annual Review of Materials Research*, **32**, 321–346.
- [12] Vineyard, G.H. (1957) Frequency factors and isotope effects in solid state rate processes. *Journal of Physics and Chemistry of Solids*, **3**, 121–127.
- [13] Weiner, J.H. (2002) *Statistical Mechanics of Elasticity*, Dover, New York.
- [14] Mishin, Y., Farkas, D., Mehl, M.J., and Papaconstantopoulos, D.A. (1999) Interatomic potentials for monoatomic metals from experimental data and *ab initio* calculations. *Physical Review B*, **59**, 3393–3407.
- [15] Zhu, T., Li, J., Samanta, A. *et al.* (2007) Interfacial plasticity governs strain rate sensitivity and ductility in nanostructured metals. *Proceedings of the National Academy of Sciences of the United States of America*, **104**, 3031–3036.
- [16] Zhu, T., Li, J., and Yip, S. (2005) Nanomechanics of crack front mobility. *Journal of Applied Mechanics, Transactions ASME*, **72**, 932–935.
- [17] Asaro, R.J. and Suresh, S. (2005) Mechanistic models for the activation volume and rate sensitivity in metals with nanocrystalline grains and nano-scale twins. *Acta Materialia*, **53**, 3369–3382.
- [18] Lu, L., Zhu, T., Shen, Y.F. *et al.* (2009) Stress relaxation and the structure size-dependence of plastic deformation in nanotwinned copper. *Acta Materialia*, **57**, 5165–5173.
- [19] Cahn, J.W. and Nabarro, F.R.N. (2001) Thermal activation under shear. *Philosophical Magazine A*, **81**, 1409–1426.
- [20] Mott, N.F. (1948) Slip at grain boundaries and grain growth in metals. *Proceedings of the Physical Society of London*, **60**, 391–394.
- [21] Zhu, T., Li, J., Samanta, A. *et al.* (2008) Temperature and strain-rate dependence of surface dislocation nucleation. *Physical Review Letters*, **100**, 025502.
- [22] Warner, D.H. and Curtin, W.A. (2009) Origins and implications of temperature-dependent activation energy barriers for dislocation nucleation in face-centered cubic metals. *Acta Materialia*, **57**, 4267–4277.
- [23] Hara, S. and Li, J. (2010) Adaptive strain-boost hyperdynamics simulations of stress-driven atomic processes. *Physical Review B*, **82**, 184114.
- [24] Ryu, S., Kang, K., and Cai, W. (2011) Entropic effect on the rate of dislocation nucleation. *Proceedings of the National Academy of Sciences of the United States of America*, **108**, 5174–5178.
- [25] Meyer, W. and Neldel, H. (1937) Über die Beziehungen zwischen der Energiekonstanten  $\epsilon$  und der Mengenkosten  $a$  der Leitwert-Temperaturformel bei oxydischen Halbleitern. *Zeitschrift für Technische Physik*, **12**, 588–593.
- [26] Yelon, A., Movaghar, B., and Branz, H.M. (1992) Origin and consequences of the compensation (Meyer–Neldel) law. *Physical Review B*, **46**, 12244–12250.
- [27] Yelon, A. and Movaghar, B. (1990) Microscopic explanation of the compensation (Meyer–Neldel) rule. *Physical Review Letters*, **65**, 618–620.
- [28] Yelon, A., Movaghar, B., and Crandall, R.S. (2006) Multi-excitation entropy: its role in thermodynamics and kinetics. *Reports on Progress in Physics*, **69**, 1145–1194.
- [29] Rice, J.R. and Thomson, R. (1974) Ductile versus brittle behavior of crystals. *Philosophical Magazine*, **29**, 73–97.
- [30] Rice, J.R. and Beltz, G.E. (1994) The activation-energy for dislocation nucleation at a crack. *Journal of the Mechanics and Physics of Solids*, **42**, 333–360.
- [31] Xu, G., Argon, A.S., and Ortiz, M. (1995) Nucleation of dislocations from crack tips under mixed-modes of loading – implications for brittle against ductile behavior of crystals. *Philosophical Magazine A*, **72**, 415–451.
- [32] Zhu, T., Li, J., and Yip, S. (2004) Atomistic study of dislocation loop emission from a crack tip. *Physical Review Letters*, **93**, 025503.
- [33] Wiederhorn, S.M. (1967) Influence of water vapor on crack propagation in soda-lime glass. *Journal of the American Ceramic Society*, **50**, 407–414.
- [34] Michalske, T.A. and Freiman, S.W. (1982) A molecular interpretation of stress-corrosion in silica. *Nature*, **295**, 511–512.
- [35] Zhu, T., Li, J., Lin, X., and Yip, S. (2005) Stress-dependent molecular pathways of silica–water reaction. *Journal of the Mechanics and Physics of Solids*, **53**, 1597–1623.
- [36] Lu, L., Shen, Y.F., Chen, X.H. *et al.* (2004) Ultrahigh strength and high electrical conductivity in copper. *Science*, **304**, 422–426.
- [37] Lu, L., Schwaiger, R., Shan, Z.W. *et al.* (2005) Nano-sized twins induce high rate sensitivity of flow stress in pure copper. *Acta Materialia*, **53**, 2169–2179.

- [38] Jin, Z.H., Gumbsch, P., Ma, E. *et al.* (2006) The interaction mechanism of screw dislocations with coherent twin boundaries in different face-centred cubic metals. *Scripta Materialia*, **54**, 1163–1168.
- [39] Huang, S., Zhang, S.L., Belytschko, T. *et al.* (2009) Mechanics of nanocrack: fracture, dislocation emission, and amorphization. *Journal of the Mechanics and Physics of Solids*, **57**, 840–850.
- [40] Lawn, B. (1993) *Fracture of Brittle Solids*, Cambridge University Press, Cambridge.
- [41] Stillinger, F.H. and Weber, T.A. (1985) Computer-simulation of local order in condensed phases of silicon. *Physical Review B*, **31**, 5262–5271.
- [42] Thomson, R., Hsieh, C., and Rana, V. (1971) Lattice trapping of fracture cracks. *Journal of Applied Physics*, **42**, 3154–3160.
- [43] Kushima, A., Lin, X., Li, J. *et al.* (2009) Computing the viscosity of supercooled liquids. *Journal of Chemical Physics*, **130**, 224504.
- [44] Kushima, A., Lin, X., Li, J. *et al.* (2009) Computing the viscosity of supercooled liquids. II. Silica and strong–fragile crossover behavior. *Journal of Chemical Physics*, **131**, 164505.
- [45] Li, J., Kushima, A., Eapen, J. *et al.* (2011) Computing the viscosity of supercooled liquids: Markov network model. *PLoS ONE*, **6**, e17909.
- [46] Lau, T.T., Kushima, A., and Yip, S. (2010) Atomistic simulation of creep in a nanocrystal. *Physical Review Letters*, **104**, 175501.
- [47] Voter, A.F. (1997) Hyperdynamics: accelerated molecular dynamics of infrequent events. *Physical Review Letters*, **78**, 3908–3911.
- [48] Laio, A. and Parrinello, M. (2002) Escaping free-energy minima. *Proceedings of the National Academy of Sciences of the United States of America*, **99**, 12562–12566.
- [49] Laio, A. and Gervasio, F.L. (2008) Metadynamics: a method to simulate rare events and reconstruct the free energy in biophysics, chemistry and material science. *Reports on Progress in Physics*, **71**, 126601.
- [50] Angell, C.A. (1988) Perspective on the glass-transition. *Journal of Physics and Chemistry of Solids*, **49**, 863–871.
- [51] Klueh, R.L. (2005) Elevated temperature ferritic and martensitic steels and their application to future nuclear reactors. *International Materials Reviews*, **50**, 287–310.
- [52] Lootens, D., Hebraud, P., Lecolier, E., and Van Damme, H. (2004) Gelation, shear-thinning and shear-thickening in cement slurries. *Oil & Gas Science and Technology-Revue De L'Institut Francais Du Petrole*, **59**, 31–40.
- [53] Kabir, M., Lau, T.T., Rodney, D. *et al.* (2010) Predicting dislocation climb and creep from explicit atomistic details. *Physical Review Letters*, **105**, 095501.
- [54] Fan, Y., Kushima, A., and Yildiz, B. (2010) Unfaulting mechanism of trapped self-interstitial atom clusters in bcc Fe: a kinetic study based on the potential energy landscape. *Physical Review B*, **81**, 104102.
- [55] Fan, Y., Kushima, A., Yip, S., and Yildiz, B. (2011) Mechanism of void nucleation and growth in bcc Fe: atomistic simulations at experimental time scales. *Physical Review Letters*, **106**, 125501.
- [56] Ciccotti, M. (2009) Stress-corrosion mechanisms in silicate glasses. *Journal of Physics D: Applied Physics*, **42**, 214006.
- [57] Pellenq, R.J.M., Kushima, A., Shahsavari, R. *et al.* (2009) A realistic molecular model of cement hydrates. *Proceedings of the National Academy of Sciences of the United States of America*, **106**, 16102–16107.